Global linear stability analysis of jets in cross-flow

Marc A. Regan[1] and Krishnan Mahesh[1,†]

[1]Department of Aerospace Engineering and Mechanics, University of Minnesota, Minneapolis, MN 55455, USA

The stability of low-speed jets in cross-flow (JICF) is studied using tri-global linear stability analysis (GLSA). Simulations are performed at a Reynolds number of 2000, based on the jet exit diameter and the average velocity. A time stepper method is used in conjunction with the implicitly restarted Arnoldi iteration method. GLSA results are shown to capture the complex upstream shear-layer instabilities. The Strouhal numbers from GLSA match upstream shear-layer vertical velocity spectra and dynamic mode decomposition from simulation (Iyer & Mahesh, *J. Fluid Mech.*, vol. 790, 2016, pp. 275–307) and experiment (Megerian *et al.*, *J. Fluid Mech.*, vol. 593, 2007, pp. 93–129). Additionally, the GLSA results are shown to be consistent with the transition from absolute to convective instability that the upstream shear layer of JICFs undergoes between $R = 2$ to $R = 4$ observed by Megerian *et al.* (*J. Fluid Mech.*, vol. 593, 2007, pp. 93–129), where $R = \bar{v}_{jet}/u_\infty$ is the jet to cross-flow velocity ratio. The upstream shear-layer instability is shown to dominate when $R = 2$, whereas downstream shear-layer instabilities are shown to dominate when $R = 4$.

Key words: absolute/convective instability, jets, turbulent flows

1. Introduction

Jets in cross-flow (JICF), or transverse jets, are a canonical flow where a jet of fluid is injected normal to a cross-flow. An incoming flat-plate boundary layer interacts with a wall-normal jet, creating a complex array of inter-related vortical structures. The shear-layer vortices and the Kelvin–Helmholtz instability are typically observed on the upstream side of the jet. The counter-rotating vortex pair (CVP), which dominates the jet cross-section (Kamotani & Greber 1972; Smith & Mungal 1998), persists far downstream and is a characteristic feature of transverse jets. Additionally, horseshoe vortices are formed near the wall just upstream of the jet exit and wrap around the jet (Krothapalli, Lourenco & Buchlin 1990; Kelso & Smits 1995). As the horseshoe vortices travel downstream they begin to tilt upward during 'separation events' (Fric & Roshko 1994) caused by the adverse pressure gradient created as the jet entrains fluid from the boundary layer. This process forms wake vortices that extend up in the wall-normal direction through the jet wake (Fric & Roshko 1994; Eiff, Kawall & Keffer 1995; Kelso, Lim & Perry 1996; McMahon, Hester & Palfery 1971; Moussa, Trischka & Eskinazi 1977). Transverse jets may be found in

† Present address: 110 Union St. SE, 107 Akerman Hall, Minneapolis, MN 55455, USA.
Email address for correspondence: kmahesh@umn.edu

many real-world engineering applications including: gas turbine combustor dilution jets, film cooling, vertical and/or short take-off and landing (V/STOL) aircraft and thrust vectoring. Reviews by Margason ([1993]), Karagozian ([2010]) and Mahesh ([2013]) compile most of this research, both experimentally and computationally, over the last seven decades.

The JICF may be characterized by the following parameters: the jet Reynolds number,

$$Re = \overline{v}_{jet}D/v_{jet}, \tag{1.1}$$

based on the average velocity ($\overline{v}_{jet}$) at the jet exit, the diameter (D), and the kinematic viscosity of the jet (v_{jet}); the cross-flow Reynolds number,

$$Re_{\infty} = u_{\infty}D/v, \tag{1.2}$$

based on the free-stream velocity (u_{∞}) and kinematic viscosity of cross-flow (v); the momentum flux ratio,

$$J = \rho_{jet}\overline{v}_{jet}^2/\rho_{\infty}u_{\infty}^2, \tag{1.3}$$

where ρ_{jet} and ρ_{∞} are the density of the jet and free stream, respectively. When the jet and free-stream densities are equal, as in isodensity flows, the jet to cross-flow velocity ratio is appropriate and is defined as,

$$R = \overline{v}_{jet}/u_{\infty}. \tag{1.4}$$

This ratio can also be defined as,

$$R^* = \frac{v_{jet,max}}{u_{\infty}} \tag{1.5}$$

based on the maximum velocity at the jet exit. The present work considers low-speed jets in cross-flow that are isodensity, and R is used as the characterization parameter.

Megerian *et al.* ([2007]) performed experiments on the JICF at Re of 2000 and 3000 over the range $1 \leqslant R \leqslant 10$. They collected vertical velocity spectra along the upstream shear layer and observed this region to transition from absolutely to convectively unstable between $R = 2$ and $R = 4$. When $R = 2$, Megerian *et al.* ([2007]) observed in the upstream shear layer a strong tone at a single Strouhal number ($St = fD/v_{jet,max}$), based on the jet exit diameter (D) and the maximum velocity at the jet exit ($v_{jet,max}$). This disturbance originated near the jet exit and was also observed further downstream. This is consistent with an absolute instability, which grows at the point of origin and travels downstream. Conversely, when $R = 4$ Megerian *et al.* ([2007]) observed that upstream shear-layer instabilities are weaker and a broader spectrum formed further downstream. This behaviour is consistent with a convective instability, which grows as it travels downstream.

Iyer & Mahesh ([2016]) performed direct numerical simulations (DNS) matching the experimental set-up of Megerian *et al.* ([2007]) and were able to capture the complex shear-layer instability. Vertical velocity spectra from simulation show good agreement with experiment and observed the same stability transition between $R = 2$ and $R = 4$. In an effort to further understand this transition, Iyer & Mahesh ([2016]) suggested that the leading edge shear layer is actually a counter-current shear layer.

According to the classic analysis by Huerre & Monkewitz (1985), the following velocity ratio characterizes the stability of counter-current mixing layers:

$$Q = \frac{V_1 - V_2}{V_1 + V_2}, \tag{1.6}$$

where V_1 and V_2 are the velocities of the two mixing layers. Huerre & Monkewitz (1985) show that for $Q > 1.315$ a mixing layer is absolutely unstable, whereas if $Q < 1.315$ the mixing layer is convectively unstable. Iyer & Mahesh (2016) calculated Q from their simulation for $R = 2$ and $R = 4$. The mixing layer velocities were taken as the maximum and minimum (most negative) vertical velocities across the upstream shear layer of the turbulent mean flows. Iyer & Mahesh (2016) found that $Q = 1.44$ and $Q = 1.20$ for $R = 2$ and $R = 4$, respectively. This suggests that the mechanism that drives the stability for free shear layers may also drive stability characteristics for complex flows like the JICF.

Furthermore, experiments of Narayanan, Barooah & Cohen (2003) have shown that when $R = 6$, low-amplitude excitation of JICFs that have convectively unstable upstream shear layers could promote mixing. Conversely, M'Closkey *et al.* (2002) and Shapiro *et al.* (2006) have shown that when $R \leqslant 4$, high-amplitude excitation has little success increasing jet penetration or mixing. These results highlight the importance of furthering our understanding of the upstream shear layer's transition from absolutely to convectively unstable, due to the effect on which control strategies are most successful.

Alves, Kelly & Karagozian (2008) have studied the stability of JICFs using local linear stability analysis. They study the spatial stability of two different base flows; a modified version of the potential flow solution by Coelho & Hunt (1989) and continuous velocity model based on the same potential flow solution (valid for larger values of Strouhal number). In their analysis they prescribe a temporal wavenumber, ω, which is real (i.e. zero growth rate), and solve for the complex spatial wavenumber, α.

The linear stability of the JICF has been studied by Bagheri *et al.* (2009), which marks one of the first simulation-based tri-global linear stability analysis (LSA) of a fully three-dimensional base flow. From this point on, global LSA (GLSA) will refer to tri-global linear stability analysis unless otherwise specified. Bagheri *et al.* (2009) studied the stability of the JICF at a jet to cross-flow velocity ratio $R^* = 3$ (1.5), with a Reynolds number $Re_{\delta_0^*} = U_\infty \delta_0^* / \nu = 165$, based on the displacement thickness δ_0^* at the inlet of the cross-flow, or equivalently $Re_{cf} = Du_\infty / \nu_\infty = 495$, based on the jet exit diameter D. The steady base flow at this value of R^* was obtained using selective frequency damping (SFD) (Åkervik *et al.* 2006). The jet nozzle was not included in their simulation and a parabolic velocity profile from pipe Poiseuille flow was imposed at the jet exit. Unstable high-frequency modes associated with the upstream shear layer as well as lower-frequency wake modes were identified in their work. Additionally, it was shown that the shedding frequency for the upstream shear layer was not far from the nonlinear shedding frequency. However, the linear wake mode frequency was far from the nonlinear wake frequency. Bagheri *et al.* (2009) suggested that the differences in shedding frequencies could be related to the differences between the SFD solution and the time-averaged solution.

Peplinski, Schlatter & Henningson (2015) extended upon the analysis of Bagheri *et al.* (2009) to include $R^* = 1.5$ and $R^* = 1.6$. Peplinski *et al.* (2015) used modal and non-modal linear analysis to study the JICF. They observed an almost identical wavepacket develop for the stable ($R^* = 1.5$) and unstable ($R^* = 1.6$) cases, and were able to determine the bifurcation point of R^* to lie between 1.5 and 1.6.

In the present work, the stability of the JICF is studied using GLSA of the turbulent mean flow. To the best of our knowledge, the grid resolution and size of the eigenvalue problem for GLSA go beyond what has been reported in the literature. The jet nozzle is included in our simulation and matches the experimental nozzle used by Megerian *et al.* (2007), which is designed to produce a top-hat profile at the jet exit. When performing DNS of the JICF, it is very computationally expensive to solve the tri-global eigenvalue problem directly. For example, using a grid with 80 million elements poses an eigenvalue problem with a dimension of 240 million. A variant of the Arnoldi iteration method (Arnoldi 1951) is therefore used to efficiently calculate the leading eigenvalues and their associated eigenmodes.

In §2 the numerics used for DNS (§2.1) and LSA (§2.2) are discussed. The validation cases for GLSA are described in §3. Next, §4 provides an overview of the computational set-up for studying the JICF. Section 5 highlights the results from GLSA, along with an in-depth analysis of the GLSA eigenmodes. Concluding the paper is §6 which includes a brief summary and discussion of the presented results as well as some applications to control.

2. Numerical methodology

The numerical method in the unstructured fluid solver is briefly discussed. Next, an overview of modal linear stability analysis and details regarding the iterative eigenvalue solver are provided.

2.1. *Direct numerical simulation*

Simulations are performed using an unstructured, finite-volume algorithm developed by Mahesh, Constantinescu & Moin (2004) for solving the incompressible Navier–Stokes (N–S) equations:

$$\frac{\partial u_i}{\partial t} + \frac{\partial}{\partial x_j} u_i u_j = -\frac{\partial p}{\partial x_i} + \nu \frac{\partial^2 u_i}{\partial x_j \partial x_j}, \qquad \frac{\partial u_i}{\partial x_i} = 0, \qquad (2.1a,b)$$

where ν is the kinematic viscosity of the fluid. The spatial discretization emphasizes discrete kinetic energy conservation, which allows for the simulation of complex flows at high Reynolds numbers without added numerical dissipation. Adams–Bashforth second-order time integration is used to advance the predictor velocities through the momentum equation. A Poisson equation for pressure is then derived by taking the divergence of the momentum equation and satisfying continuity. This is used in a corrector step to project the solution onto a divergence-free velocity field.

The algorithm has been validated for a variety of canonical and complex flows, including: a gas turbine combustor (Mahesh *et al.* 2004), free jet entrainment (Babu & Mahesh 2004) and transverse jets (Muppidi & Mahesh 2005, 2007, 2008; Sau & Mahesh 2007, 2008).

2.2. *Linear stability analysis*

Modal LSA is the study of the dynamic response of a base state (i.e. base flow) subject to external perturbations (see Theofilis (2011) for a review). In the present work, the incompressible Navier–Stokes equations (2.1) are linearized about a base state, $\bar{u}_i$ and $\bar{p}$. The base state can be assumed to vary arbitrarily in space. If the flow field is decomposed into a base state subject to a small $O(\varepsilon)$ perturbation,

$$\boldsymbol{u}_i = \bar{\boldsymbol{u}}_i + \varepsilon \tilde{\boldsymbol{u}}_i, \qquad p = \bar{p} + \varepsilon \tilde{p}, \qquad (2.2a,b)$$

the governing equations (2.1) can be linearized by neglecting the ε^2 terms. Additionally, if the base state is a solution to the incompressible Navier–Stokes equations (2.1), the base flow equations can be subtracted. This yields the linearized Navier–Stokes (LNS) equations:

$$\frac{\partial \tilde{u}_i}{\partial t} + \frac{\partial}{\partial x_j}\tilde{u}_i\overline{u}_j + \frac{\partial}{\partial x_j}\overline{u}_i\tilde{u}_j = -\frac{\partial \tilde{p}}{\partial x_i} + \nu\frac{\partial^2 \tilde{u}_i}{\partial x_j \partial x_j}, \qquad \frac{\partial \tilde{u}_i}{\partial x_i} = 0. \qquad (2.3a,b)$$

Note that the same numerical techniques are used to solve the LNS equations (2.3) and the N–S equations (2.1). A molecular viscosity is used to obtain both the base flow and in LSA since the base flow is obtained from DNS where all relevant scales are directly resolved and no subgrid-scale model is used.

The LNS equations (2.3) may be rewritten as a system of linear equations,

$$\frac{\partial \tilde{u}_i}{\partial t} = \boldsymbol{A}\tilde{u}_i, \qquad (2.4)$$

where $\boldsymbol{A}$ is the LNS operator and $\tilde{u}_i$ is the divergence-free velocity perturbation field. In modal LSA, our interest is in the long-time behaviour of $\tilde{u}_i$. Consequently, the solutions to the linear system of equations (2.4) are of the form:

$$\tilde{u}_i(x, y, z, t) = \sum_\omega \hat{u}_i(x, y, z)\,\mathrm{e}^{\omega t} + \mathrm{c.c.}, \qquad (2.5)$$

where ω and $\hat{u}_i$ can be complex. This defines the $\mathrm{Re}(\omega)$ as the growth/damping rate and the $\mathrm{Im}(\omega)$ as the temporal frequency of the complex velocity coefficient ($\hat{u}_i$). Substituting the ansatz (2.5) into the LNS system (2.4) transforms the system of equations into a linear eigenvalue problem,

$$\boldsymbol{\Omega}\hat{U}_i = \boldsymbol{A}\hat{U}_i, \qquad (2.6)$$

where $\omega_j = \mathrm{diag}(\boldsymbol{\Omega})_j$ is the jth eigenvalue and $\hat{u}_i^j = \boldsymbol{U}_i[j, :]$ is the jth eigenvector (i.e. eigenmode). For GLSA, the size of the eigenvalue problem (2.6) can be $O(10^6$–$10^8)$. This makes solving the eigenvalue problem using direct methods very computationally expensive, often prohibitively so. Instead, an extension of the Arnoldi iteration method (Arnoldi 1951) called the implicitly restarted Arnoldi method (IRAM), a matrix-free method, is used. The present work makes use of the IRAM implemented in the open-source P_ARPACK library (Lehoucq, Sorensen & Yang 1997) to efficiently calculate the leading (i.e. most unstable) eigenvalues and their associated eigenmodes.

A temporal exponential transformation of the eigenvalue spectrum is then performed. This transforms the most unstable eigenvalues into the most dominant (i.e. largest magnitude) eigenvalues, which P_ARPACK can solve for efficiently. To do this, the eigenvalue problem (2.6) is integrated over some time, τ:

$$\int_0^\tau \boldsymbol{\Omega}\hat{U}_i\,\mathrm{d}t = \int_0^\tau \boldsymbol{A}\hat{U}_i\,\mathrm{d}t. \qquad (2.7)$$

This yields the exponential of the eigenvalue problem (2.6):

$$\mathrm{e}^{\boldsymbol{\Omega}\tau}\hat{U}_i = \mathrm{e}^{\boldsymbol{A}\tau}\hat{U}_i, \qquad (2.8)$$

which can be rewritten as:

$$\boldsymbol{\Sigma}\hat{\boldsymbol{U}}_i = \boldsymbol{B}\hat{\boldsymbol{U}}_i, \tag{2.9}$$

where $\sigma_j = \mathrm{diag}(\boldsymbol{\Sigma})_j$. The matrix exponential $\boldsymbol{B} = \mathrm{e}^{\boldsymbol{A}\tau}$ is a time integration operator, which acts as a numerical simulation of the LNS equations (2.3) over a time τ. This method is therefore called a time stepper method. Note that between the two eigenvalue problems (2.6), (2.9), the eigenvectors, $\hat{\boldsymbol{U}}_i$, are the same. However, the eigenvalues of the original problem (2.6) must be recovered using the following relationship:

$$\omega_j = \frac{1}{\tau}\ln\sigma_j. \tag{2.10}$$

When using a time stepper method, the choice of the integration time τ is dependent on the time scales of interest for the problem at hand. It is imperative that τ is less than the smallest time scales t_s of interest; usually $\tau = t_s/2$ is appropriate. As for capturing the largest time scales t_L of interest, the number of Arnoldi vectors N_A is important. Once τ is determined, the number of Arnoldi vectors must be greater than t_L/τ; usually $N_A > 2t_L/\tau$ is appropriate. Overall, some knowledge of the range of time scales is needed to effectively use the IRAM in conjunction with a time stepper method. Additionally, note that performing stability analysis on problems with a large range of time scales can drastically effect the computational cost and storage requirements as each Arnoldi vector must be stored for each Arnoldi iteration.

For increasingly complex and globally unstable flows, a steady-state solution may be difficult and computationally expensive to obtain. As modal stability analysis looks to study the stability of more interesting problems, other approaches are being taken to solve for base states. SFD may be used to solve for a steady-state solution. This is achieved by adding a forcing term to the right-hand side, which acts as a temporal low-pass filter. Some knowledge of the lowest unstable frequency is required when choosing the filter width. In order to converge to a steady solution, the filter cutoff frequency must be lower than that of all of the flow instabilities. Although this method lends itself to easy implementation, the computational cost is governed by the range of time scales. Additionally, SFD fails to damp instabilities that are non-oscillatory, as shown by Vyazmina (2010).

Another option is to use a turbulent mean flow as a base state. Perhaps the best known example where LSA about the turbulent mean flow succeeds over the steady-state solution is the oscillating wake of a circular cylinder; which agree at onset, but LSA about the steady-state solution fails to capture the observed vortex shedding frequency far away from the bifurcation. Recent studies by Turton, Tuckerman & Barkley (2015) and Tammisola & Juniper (2016) look to further our understanding of what it means to perform GLSA around a turbulent mean flow. Additionally, Barkley (2006) and Turton *et al.* (2015) show that performing a LSA around a turbulent mean flow results in eigenvalues which have small real parts and non-zero imaginary frequencies.

Since a turbulent mean flow is a solution to the Reynolds-averaged N–S equations, a nonlinear Reynolds stress term is effectively added to the LNS equations when the base flow equations are removed (2.1)–(2.3). This translates into a mode-dependent Reynolds stress being present in the eigenvalue problem (2.6). A scale-separation argument, first introduced by Crighton & Gaster (1976), and more recently discussed in the review by Jordan & Colonius (2013), can be used to justify when the

Case	Flow	Re	Reference(s)
Parallel flow	Blasius boundary layer	580	Criminale *et al.* (2003)
Bi-global	2-D lid-driven cavity	200	Ding & Kawahara (1998)
Tri-global	3-D lid-driven cavity	1000	Gómez *et al.* (2014), Giannetti, Luchini & Marino (2009)
Tri-global	Laminar channel flow	1000	Juniper, Hanifi & Theofilis (2014)

TABLE 1. Descriptions of the cases used for validation.

mode-dependent Reynolds stress term is negligible. Only for the modes of interest (typically low frequency and large scale) must the Reynolds stress term be shown to be unimportant. For turbulent problems, multiple orders of magnitude can separate the time and length scales of turbulent motions (t_η and η, respectively) with the motions of interest (L and t_L, respectively). Relationships between turbulent and large-scale motions of interest can be determined from the Kolmogorov scales as seen in Pope (2000, pp. 186):

$$L/\eta = Re^{3/4}, \quad t_L/t_\eta = Re^{1/2}. \qquad (2.11a,b)$$

Therefore, if the scale-separation argument is to hold, there must be a significant gap between scales of interest for GLSA and the turbulent motions themselves. It can be shown by using the relationships above (2.11) that using a turbulent mean flow as a base state in GLSA may provide meaningful physical insight with respect to stability.

3. Validation

The LSA capability developed for the present work is validated in this section. Table 1 outlines the validation cases for the present work. First, parallel flow LSA of a Blasius boundary layer subject to a streamwise Tollmien–Schlichting (T–S) wave is compared to the results of Criminale, Jackson & Joslin (2003). Second, bi-global LSA of a two-dimensional (2-D) lid-driven cavity with a spanwise wave disturbance is compared to the work of Ding & Kawahara (1998). Next, GLSA of a 3-D lid-driven cavity is validated against Gómez, Gómez & Theofilis (2014). Finally, GLSA of laminar channel flow is compared to the classic parallel flow LSA results for Poiseuille flow.

3.1. *Parallel flow LSA*

Parallel flow LSA assumes wave-like homogeneity in time and two spatial directions. This allows for the governing equations to be simplified to an ordinary differential equation, which reduces the computational cost of solving the associated LSA eigenvalue problem. Here, the stability of a Blasius boundary layer is chosen as a validation case due to its simplicity and the extensive analysis in the literature. For this problem the spanwise and streamwise directions are assumed to be homogeneous.

Criminale *et al.* (2003) provide temporal LSA results for a Blasius boundary layer subject to a streamwise T–S disturbance. The applied T–S disturbance has a wavenumber $\alpha = 0.179$ and is applied at $Re = 580$, based on the boundary layer thickness. The eigenvalue problem corresponding to the Orr–Sommerfeld equations

Re	α	Criminale *et al.* (2003)	Present
580	0.179	$0.007970 + i0.3641$	$0.007835 + i0.3657$
		$-0.2787 + i0.2897$	$-0.2765 + i0.2922$
		$-0.1921 + i0.4839$	$-0.1925 + i0.4862$
		$-0.3653 + i0.5572$	$-0.3648 + i0.5597$
		$-0.3308 + i0.6863$	$-0.3307 + i0.6885$
		$-0.4341 + i0.7937$	$-0.4334 + i0.7959$
		$-0.4147 + i0.8874$	$-0.4131 + i0.8879$

TABLE 2. The leading eigenvalues ($c_j = \omega_j/\alpha$) from parallel flow LSA results for a Blasius boundary layer at $Re = 580$, subject to a streamwise T–S wave, ($\alpha = 0.179$), compared to Criminale *et al.* (2003) for validation.

Re	β	Ding & Kawahara (1998)	Present
200	6	$-0.38 + i0.57$	$-0.38 + i0.56$
	9	$-0.54 + i0.75$	$-0.54 + i0.72$

TABLE 3. The leading eigenvalues (ω_j) from bi-global LSA of a 2-D lid-driven cavity subject to different spanwise wavenumbers (β) compared to Ding & Kawahara (1998) for validation.

is solved directly by Criminale *et al.* (2003). Conversely, in the present work the eigenvalue problem associated with the 2-D LNS (2.3) is instead solved directly for consistency throughout the validation process. The seven leading eigenvalues show good agreement with the present work as shown in table 2.

3.2. *Bi-global LSA*

A 2-D lid-driven cavity is studied using bi-global LSA. Here, time and the spanwise direction are assumed to be homogeneous. Consequently, the base state is the 2-D steady-state solution for the square lid-driven cavity at $Re = 200$, based on the cavity height and lid velocity. Two purely real (i.e. oscillatory) spanwise wavenumbers ($\beta = 6, 9$) are individually applied as perturbations to the base state. The 2-D LNS (2.3) are solved in conjunction with the time stepper method and IRAM that was outlined in § 2.2.

Results from bi-global LSA are compared with Ding & Kawahara (1998) in table 3. The leading eigenvalues for the two spanwise perturbations show good agreement with the results of Ding & Kawahara (1998).

3.3. *GLSA*

When performing GLSA, no directions are assumed to be homogeneous, which can be very computationally expensive. Only until recently have computational resources made studying the stability of complex 3-D problems practical. The stability of a 3-D lid-driven cavity has been studied by multiple authors using different numerical techniques.

The stability of a steady cubic 3-D lid-driven cavity is studied at a Reynolds number of 1000, based on the cavity height and lid velocity. Giannetti *et al.* (2009) and Gómez *et al.* (2014) have both performed GLSA of a cubic 3-D lid-driven cavity.

Re	Giannetti *et al.* (2009) (64^3)	Gómez *et al.* (2014) (144^3)	Present (288^3)
1000	$-0.1276 \pm i0.285$	$-0.1292 \pm i0.329$	$-0.1352 \pm i0.299$
	$-0.1301 \pm i0.457$	$-0.1348 \pm i0.485$	$-0.1304 \pm i0.487$
	-0.1457	-0.1382	-0.1375

TABLE 4. The leading eigenvalues (ω_j) from GLSA for a stable 3-D lid-driven cavity at $Re = 1000$ compared to Giannetti *et al.* (2009) and Gómez *et al.* (2014) for validation. The number inside of the brackets represents the number of elements in the grid that was used.

All three results were obtained using some form of the Arnoldi iteration method. Giannetti *et al.* (2009) solve the LNS (2.3) and utilize the IRAM within the ARPACK library. Conversely, Gómez *et al.* (2014) directly applies the output from a N–S (2.1) solver to generate approximate results for GLSA using the classic Arnoldi algorithm. The present work solves the LNS, but utilizes the IRAM implemented in the parallel P_ARPACK library. Results show good agreement across the different numerical methods as shown in table 4.

Furthermore, the real part of the leading eigenmodes from the present work are shown in figure 1 and highlight positive and negative isocontours of the perturbation velocity fields. Eigenmode results shown in Gómez *et al.* (2014) show good qualitative agreement with the present work. The complexity as well as the symmetry of the 3-D cavity can be seen in the eigenmode results. The third eigenmode is a stable stationary mode (i.e. non-oscillatory), and has been described by Gómez *et al.* (2014) as resembling different families of linear modes with Taylor–Görtler-like structures.

3.4. *GLSA and parallel flow LSA*

As a final point of validation, results from GLSA are compared to classic parallel flow LSA. The stability of a laminar channel is chosen because the assumption that the streamwise and spanwise directions are homogeneous holds true, making the parallel flow assumption valid.

The stability of a laminar channel at $Re = 5780$, based on the centreline velocity and channel half-height h, is first computed using GLSA. The channel half-height h is 1, while the streamwise length is 4π and the spanwise width is $4\pi/3$. Periodic boundary conditions are applied in the streamwise and spanwise directions, whereas the no-slip condition is applied at the top and bottom of the channel. Since the streamwise and spanwise wavenumbers (α and β, respectively) are not specified in GLSA, any combination of wavenumbers may be present in the GLSA results. Therefore, the jth pair of ω_j and $\hat{u}_i^j$ may have a non-zero α_j and/or β_j that can then be extracted using streamwise and spanwise fast Fourier transforms. The α_j and β_j can then be used as input into parallel flow LSA.

The non-zero components of two leading eigenmodes from GLSA are shown in figures 2(*a*,*b*) and 3(*a*). A quantitative comparison between the GLSA results and the results from parallel flow LSA are shown in figures 2(*c*) and 3(*b*). The complex Fourier coefficients, $\hat{u}_i^j$, as well as their magnitudes, are plotted against the results from parallel flow LSA. The comparison shows good agreement for both eigenmodes in all three velocity components.

The same two leading eigenvalues from GLSA and parallel flow LSA are shown in table 5. The eigenvalues are non-dimensionalized by the centreline velocity and the

(*a*) $\omega = -0.1352 \pm \mathrm{i}0.299$

$\tilde{u}$ $\tilde{v}$ $\tilde{w}$

(*b*) $\omega = -0.1304 \pm \mathrm{i}0.487$
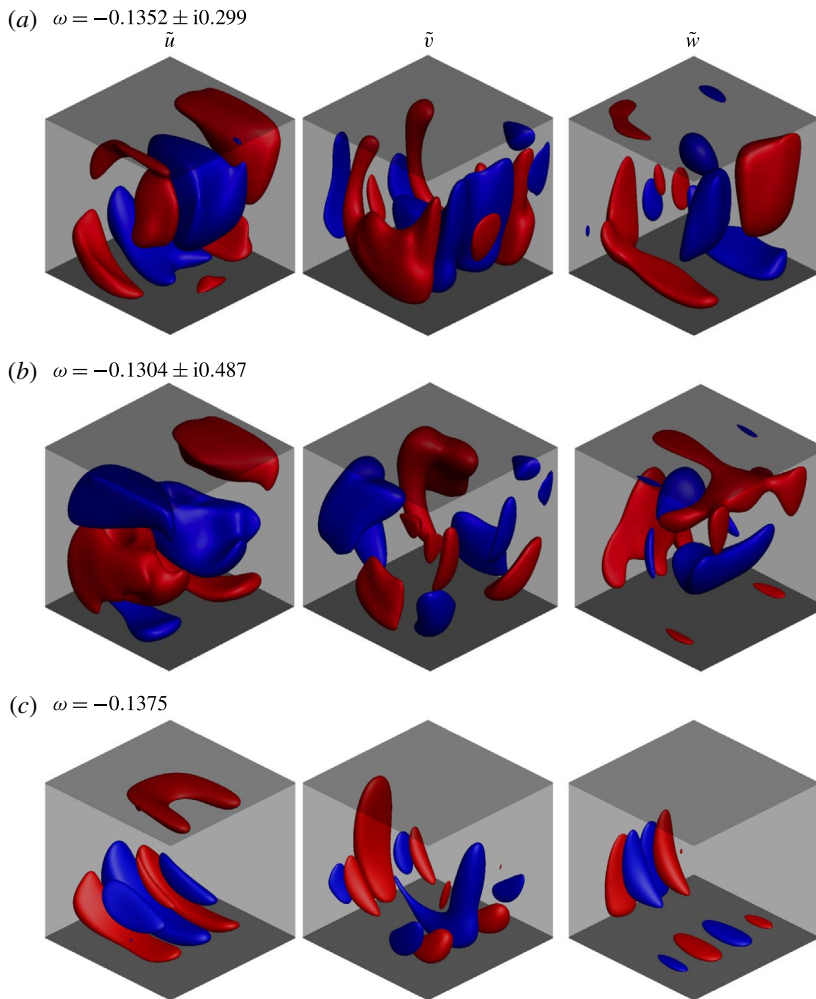

(*c*) $\omega = -0.1375$

FIGURE 1. (Colour online) Real part of the eigenmodes from GLSA for a 3-D lid-driven cavity at $Re = 1000$. The results are shown with positive and negative isocontours of $\tilde{u}, \tilde{v}, \tilde{w} = \pm 0.15$. The associated eigenvalues are shown, with the real part being the growth rate, and the imaginary part being the frequency. Modes (*a–c*) show good qualitative agreement with Gómez *et al.* (2014). A comparison to the eigenvalues results of Giannetti *et al.* (2009) and Gómez *et al.* (2014) may be found in table 4.

Re	α	β	Juniper *et al.* (2014) (Parallel flow LSA)	Present (GLSA)
1000	1	0	$-2.33610 \times 10^{-2} + \mathrm{i}9.77640 \times 10^{-1}$	$-2.33374 \times 10^{-2} \pm \mathrm{i}9.77638 \times 10^{-1}$
	1	1.5	$-2.56110 \times 10^{-2} + \mathrm{i}9.77640 \times 10^{-1}$	$-2.55906 \times 10^{-2} \pm \mathrm{i}9.77638 \times 10^{-1}$

TABLE 5. Two leading eigenvalues (ω_j) from GLSA for laminar channel flow at $Re = 1000$. Streamwise wavenumbers, α, and spanwise wavenumbers, β, are observed in the global eigenmodes (see figures 2 and 3) and are used as input to parallel flow stability analysis of Poiseuille flow. The parallel flow stability results are produced by a code available in the supplementary material from Juniper *et al.* (2014).
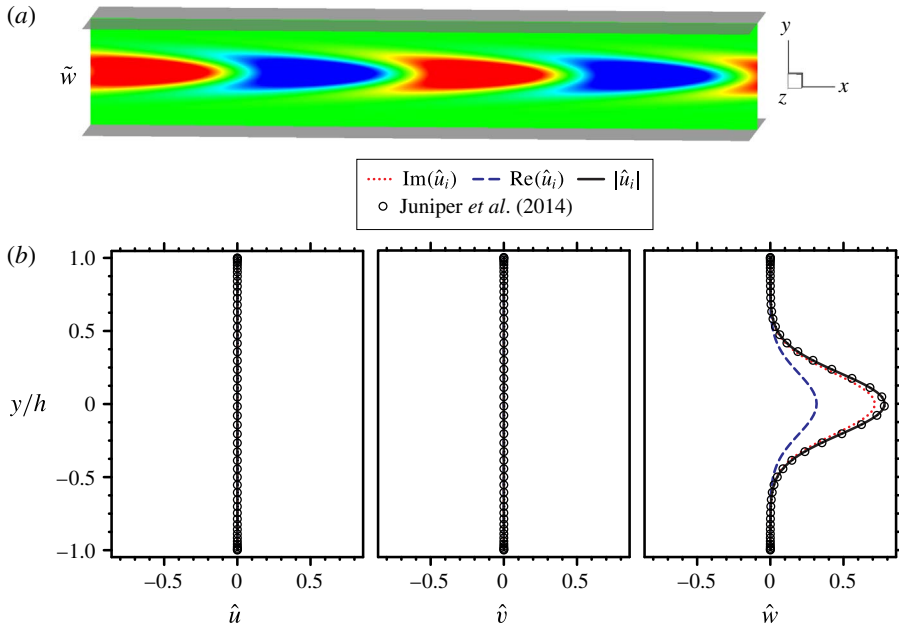
FIGURE 2. (Colour online) Shown are the real parts of the first eigenmode corresponding to the eigenvalues in table 5 from GLSA for laminar channel flow at $Re = 1000$. Periodic boundary conditions in x and z are applied. Here, there is no variation in the z-direction, making a single slice sufficient to display all relevant data. The results are shown as an x–y slice ($z = 0$) with contours of $\tilde{w}$ (note: $\tilde{u} = \tilde{v} = 0$). The streamwise and spanwise wavenumbers ($\alpha = \mathrm{i}1$, $\beta = \mathrm{i}0$) are extracted and used as input to classic parallel flow stability analysis of Poiseuille flow. Additionally, the tri-global eigenmode Fourier coefficients ($\hat{\boldsymbol{u}}_i$) are compared with the results from parallel stability of Juniper *et al.* (2014) for $|\hat{u}|$, $|\hat{v}|$ and $|\hat{w}|$. Note that every fourth point from Juniper *et al.* (2014) is plotted in an effort to not obscure other data.

channel half-height h. The agreement between the two different numerical methods, utilizing drastically different numerical techniques and different assumptions, is very strong. Reasonable agreements for growth rates and frequencies are obtained.

Thus, the present unstructured grid LSA solver can be considered validated. This LSA solver will now be used to study the GLSA of the JICF.

4. Problem description

Figure 4 shows the simulation set-up. At the inflow, a laminar Blasius boundary layer profile is prescribed. The computational grid and boundary layer profile are the same as those used by Iyer & Mahesh (2016). The boundary layer has been shown to match well with experiments at $x/D = -5.5$. The jet nozzle is located at the origin of the computational domain and is included in all simulations. It has been shown by Iyer & Mahesh (2016) that the jet nozzle plays a crucial role in setting up the mean flow near the jet exit, thus affecting the stability characteristics of the flow. A fifth-order polynomial is used to model the nozzle shape used in the experiments of Megerian *et al.* (2007). The jet exit diameter D is 3.81 mm and the average velocity at the jet exit $\overline{v}_{jet}$ is 8 m s^{-1}. Additional simulation details are outlined in table 6.
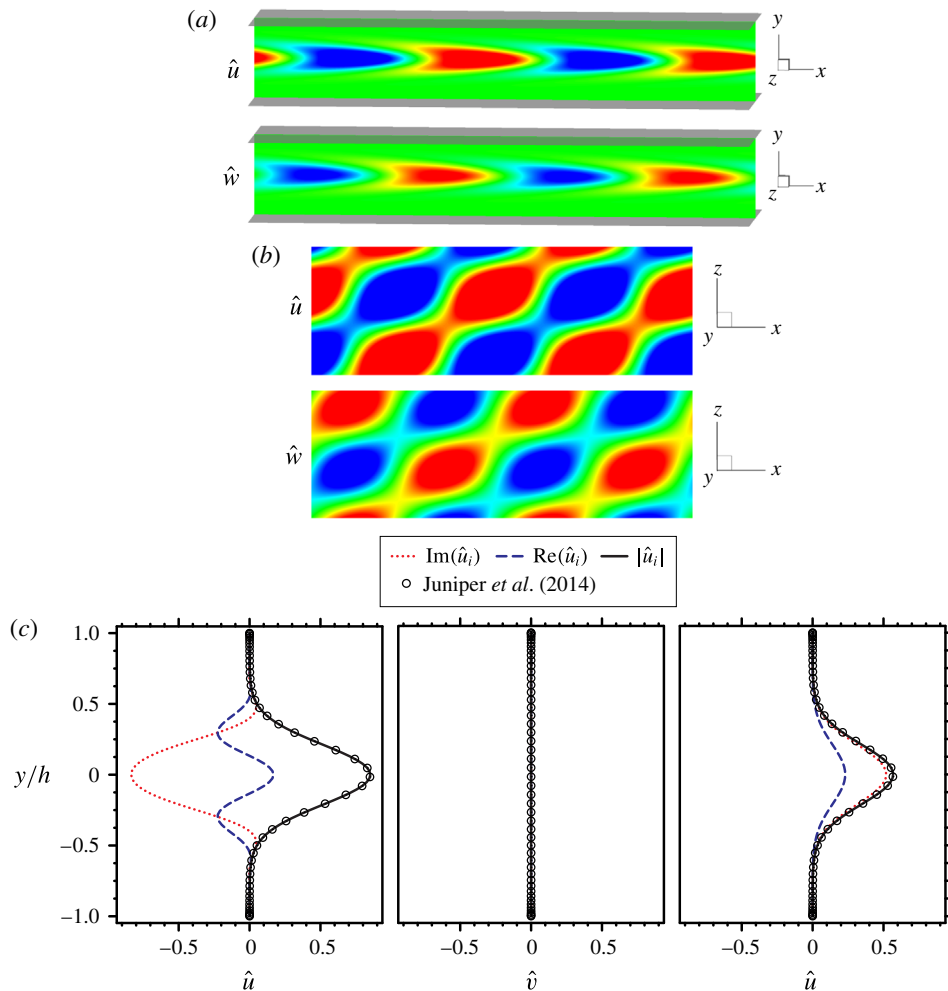
FIGURE 3. (Colour online) Similar to figure 2, shown is the real part of the second eigenmode corresponding to the eigenvalues in table 5 from GLSA for laminar channel flow at $Re = 1000$. Periodic boundary conditions in x and z are applied. Here, there is variation in the z-direction, requiring an additional slice to be shown. The results are shown as x–y ($z = 0$) and z–x ($y = 0$) slices with contours of $\tilde{u}$ and $\tilde{w}$ (note: $\tilde{v} = 0$). The streamwise and spanwise wavenumbers ($\alpha = \mathrm{i}1$ and $\beta = \mathrm{i}1.5$) may be extracted and used as input to a classic parallel flow stability analysis of Poiseuille flow. Additionally, the tri-global eigenmode Fourier coefficients ($\hat{u}_i$) are compared with the results from parallel stability of Juniper *et al.* (2014) for $|\hat{u}|$, $|\hat{v}|$ and $|\hat{w}|$. Note that every fourth point from Juniper *et al.* (2014) is plotted in an effort to not obscure other data.

Simulation cases $R2$ and $R4$ are performed at the same conditions as the experiments of Megerian *et al.* (2007).

The unstructured capabilities of the solver allow the cross-flow domain and jet nozzle to be simulated together. Figure 4 also describes the extent of the computational domain. The domain extends $8D$ upstream of the jet exit to the inflow boundary where the Blasius laminar boundary layer solution is applied. $16D$
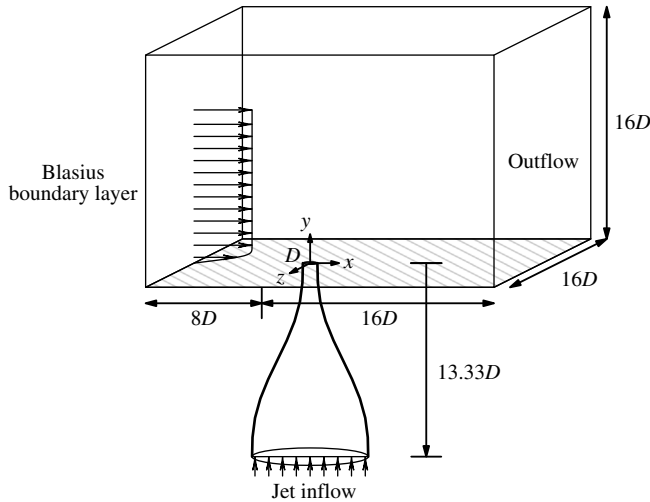
FIGURE 4. A schematic of the jet in cross-flow computational domain is shown. The origin is located at the centre of the jet exit. A Blasius boundary layer is prescribed as the leftmost inflow condition. Additionally, uniform inflow is prescribed for the jet inflow. The nozzle shape is modelled using a fifth-order polynomial that matches the nozzle used in experiments of Megerian *et al.* (2007).
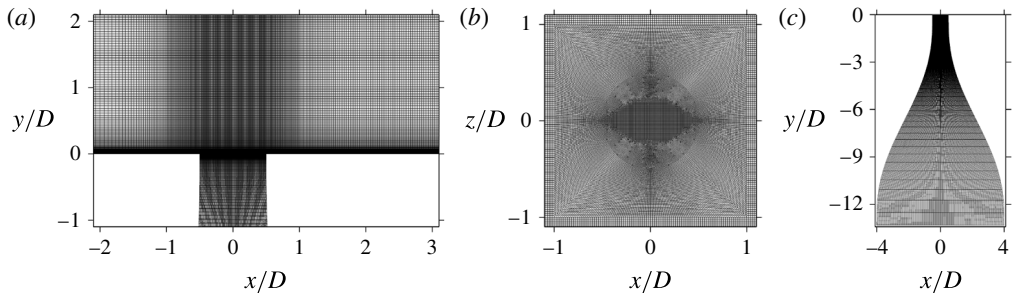

FIGURE 5. The computational grid is shown. A view of the symmetry plane (*a*) as well as a wall-normal plane near the jet exit (*b*) and the nozzle (*c*) are shown. The grid is composed of 80 million elements.

downstream of the jet exit is the outflow boundary. In addition, Neumann boundary conditions are applied to the sides located $8D$ from the origin in the spanwise directions. The simulated nozzle extends $13.33D$ below the jet orifice, at which point a uniform inflow is prescribed to achieve the correct velocity at the jet exit. The top of the domain is located $16D$ above the origin and also has a Neumann boundary condition applied.

The computational grid is shown in figure 5, and is made up of 80 million elements divided into 4096 partitions. This allows for 80 elements inside of the inflow laminar boundary layer in the *y*-direction and 400 elements around the jet exit. Downstream of the jet exit, the grid maintains a spacing of $\Delta x/D = 0.033$ and $\Delta z/D = 0.02$, with a $\Delta y_{min}/D = 0.0013$, which are finer than the spacings used by Muppidi & Mahesh (2007) to simulate a turbulent JICF. After making the assumption that downstream of the jet exit the boundary layer is turbulent, viscous wall units may be computed using
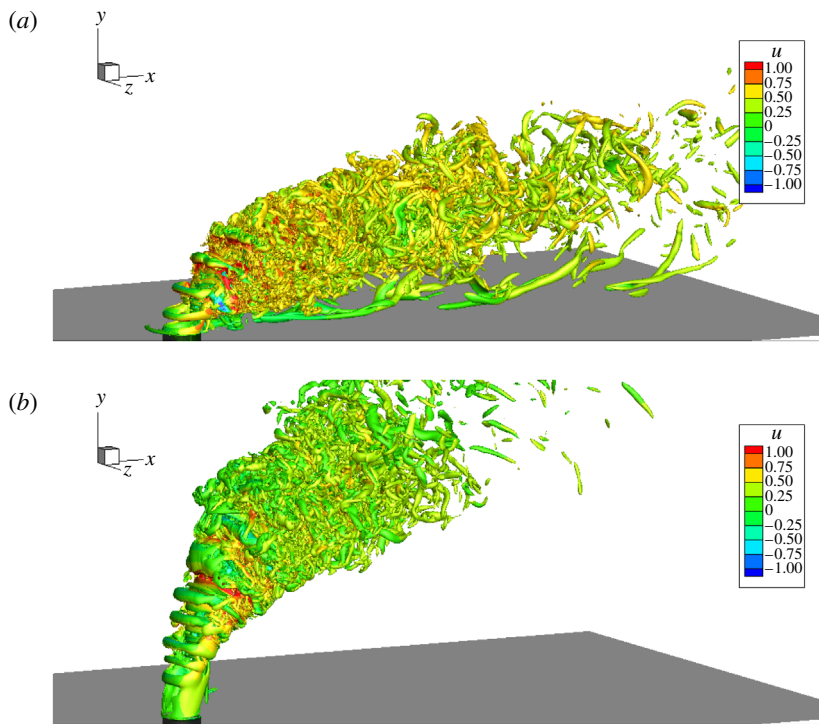
FIGURE 6. (Colour online) Isocontours of Q-criterion coloured by streamwise velocity for the instantaneous turbulent flow field for $R = 2$ (*a*) and $R = 4$ (*b*). The upstream shear-layer roll up is clear and defined for both case $R2$ and $R4$, whereas the downstream shear-layer roll up is less obvious. Additionally, long wake vortices are visible for case $R2$ near the wall. Both cases showcase fine-scale turbulent structures far downstream.

Case	$R = \bar{v}_{jet}/u_\infty$	$R^* = v_{jet,max}/u_\infty$	$Re = D\bar{v}_{jet}/\nu_{jet}$	$Re_{cf} = Du_\infty/\nu_\infty$	θ_{bl}/D
$R2$	2	2.44	2000	1000	0.1215
$R4$	4	4.72	2000	500	0.1718

TABLE 6. Details are shown for the simulations used to study the stability of the JICFs. Jet to cross-flow ratios R of 2 and 4 are studied at a Reynolds number Re of 2000, based on the average velocity $\bar{v}_{jet}$ at the jet exit and the jet exit diameter D. Also shown is the jet to cross-flow ratio R^*, based on the jet exit peak velocity $v_{jet,max}$ and the Reynolds number Re_{cf}, based on the cross-flow velocity u_∞. The momentum thickness of the laminar cross-flow boundary layer is described at the jet exit when the jet is turned off.

$c_f = 0.0576 Re_x^{-0.2}$ (Schlichting & Gersten 1979). Wall spacings may then be calculated at the outflow as $\Delta x^+/D$, $\Delta y_{min}^+/D$ and $\Delta z^+/D$, as 2.74, 0.1, and 1.66 when $R = 2$ and 1.48, 0.058 and 0.89 when $R = 4$, respectively.

Instantaneous isocontours of Q-criterion (Hunt, Wray & Moin 1988) coloured by streamwise velocity for the turbulent flow field are shown in figure 6 for case $R2$ (*a*)

and $R4$ (b). Q is defined as

$$Q = -0.5 \frac{\partial u_i}{\partial x_j} \frac{\partial u_j}{\partial x_i}. \tag{4.1}$$

The Q-criterion highlights vortex cores by representing regions where pressure is a local minimum. The complexity of the turbulent JICF is shown in these instantaneous results. Important features include the coherent upstream shear-layer roll up, as well as long string-like wake vortices near the wall. Additionally, a less visible downstream shear-layer roll up is visible that interacts with the upstream shear layer at the collapse of the potential core. Many fine-scale turbulent structures are also visible downstream in the jet wake. In the section that follows, GLSA results are discussed that provide valuable insight to the stability of these two flow configurations.

5. Results

GLSA is performed for the $R2$ and $R4$ cases described in table 6. These cases match the experimental and computational set-ups of Megerian *et al.* (2007) and Iyer & Mahesh (2016), respectively. Choosing an appropriate base flow is important for LSA. The scale-separation argument from § 2.2 provides the following results:

$$\left.\begin{aligned} L/\eta &= Re^{3/4} \approx 300, \\ t_L/t_\eta &= Re^{1/2} \approx 45. \end{aligned}\right\} \tag{5.1}$$

This shows that 1 or more orders of magnitude separate the time and length scales of turbulent motions and the motions of interest. SFD has been shown by Bagheri *et al.* (2009) to alter some important features of the JICF; specifically the collapse of the potential core and the near-wall reverse flow downstream of the jet exit. Therefore, turbulent mean flow solutions are used as the base states in GLSA for the present work.

Turbulent mean flow solutions were generated by Iyer & Mahesh (2016) using 32 000 and 39 000 samples from DNS to temporally average cases $R2$ and $R4$, respectively. Iyer & Mahesh (2016) have shown that there is good agreement between the temporally averaged solutions from simulation and experiment.

A grid convergence study was performed to study the sensitivity of the leading eigenvalue for three different grids when $R = 2$. The upstream shear-layer eigenvalue was computed for a coarse grid (10 million elements), the present work grid (80 million elements) and a finer grid (99 million elements). All three eigenvalues are shown in figure 7 and show good agreement. Peplinski *et al.* (2015) have shown that the leading eigenvalue can also be sensitive to the size of the computational domain. Iyer & Mahesh (2016) have shown that the domain size in their DNS successfully captures both the upstream boundary layer and upstream shear-layer frequencies when compared to experiment. We use the same domain length as Iyer & Mahesh (2016).

For case $R2$, the 15 leading eigenvalues were computed to a maximum residual of 1×10^{-14}. In addition, 60 Arnoldi vectors were generated for each iteration in the IRAM. The LNS (2.3) were integrated 0.114 time units (non-dimensionalized by $D/v_{jet,max}$) to generate each Arnoldi vector. This allowed for a more than adequate temporal resolution to solve for the highest frequency in the upstream shear layer, which were observed in DNS at a $St = 0.65$ (i.e. period of 1.54 time units). After generating the 60 Arnoldi vectors, they spanned 6.85 time units, allowing for the IRAM to efficiently resolve the lower-frequency wake modes as well.
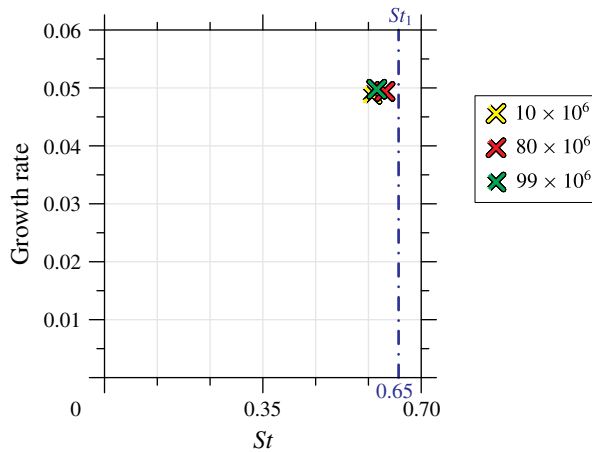
FIGURE 7. (Colour online) Results from the grid convergence study used to determine the sensitivity of the leading eigenvalue to the mesh for case $R2$. Three different grids were tested: coarse (10 million elements), present work (80 million elements), fine (99 million elements). The eigenvalues have been non-dimensionalized so that the growth rate is $\mathrm{Re}(\omega)D/(2\pi v_{jet,max})$ and the Strouhal number is $\mathrm{Im}(\omega)D/(2\pi v_{jet,max})$. St_1 highlights the primary Strouhal number observed along the upstream shear layer in simulations by Iyer & Mahesh (2016).

Similarly for case $R4$, the 16 leading eigenvalues were computed to the same maximum residual of 1×10^{-14}. In addition, 100 Arnoldi vectors were generated for each iteration in the IRAM. Time was integrated 0.157 time units (non-dimensionalized by $D/v_{jet,max}$) to generate each Arnoldi vector. This allowed for a temporal resolution that could sufficiently capture the high-frequency upstream shear-layer modes, which were observed in DNS at $St = 0.39$ and $St = 0.78$ (i.e. periods of 2.56 and 1.28 time units, respectively). Once the 60 Arnoldi vectors were generated, they spanned 15.7 time units, allowing for the IRAM to efficiently resolve lower-frequency modes.

Figure 8 shows the eigenvalue spectra obtained from GLSA for case $R2$ (*a*) and $R4$ (*b*). The eigenvalues have been non-dimensionalized so that the growth rate is $\mathrm{Re}(\omega)D/(2\pi v_{jet,max})$ and the Strouhal number is $\mathrm{Im}(\omega)D/(2\pi v_{jet,max})$. As discussed in § 2.2, Barkley (2006) and Turton *et al.* (2015) showed that when performing GLSA around a turbulent mean flow, the resulting eigenvalues have very small growth rates; which is consistent with the results in figure 8. The circled eigenvalues have Strouhal numbers closest to those found in experiments (Megerian *et al.* 2007) and simulations (Iyer & Mahesh 2016) (i.e. St_1 ($R2$), St_2 ($R4$)) when analysing vertical velocity spectra from the upstream shear layer. The eigenvalues from GLSA have Strouhal numbers associated with the upstream shear layer of 0.62 for $R2$ and 0.75 for $R4$. Comparatively, vertical velocity spectra show that Strouhal numbers of 0.65 for $R2$ and 0.78 for $R4$ dominate the upstream shear layer. Figure 9 gives an isometric view of the two eigenmodes for $R2$ (*a*) and $R4$ (*b*), that are associated with the circled eigenvalues in figure 8. Dynamic mode decomposition (DMD) modes from Iyer & Mahesh (2016) are also shown in figure 9 for $R2$ (*c,e*) and $R4$ (*d,f*). Additionally, figure 10 shows cross-sectional views of the upstream shear-layer eigenmodes and DMD modes at the symmetry plane ($z = 0$). The DMD results from Iyer & Mahesh (2016) have Strouhal numbers of 0.65 and 1.3 for $R2$ and 0.39 and 0.78 for $R4$,
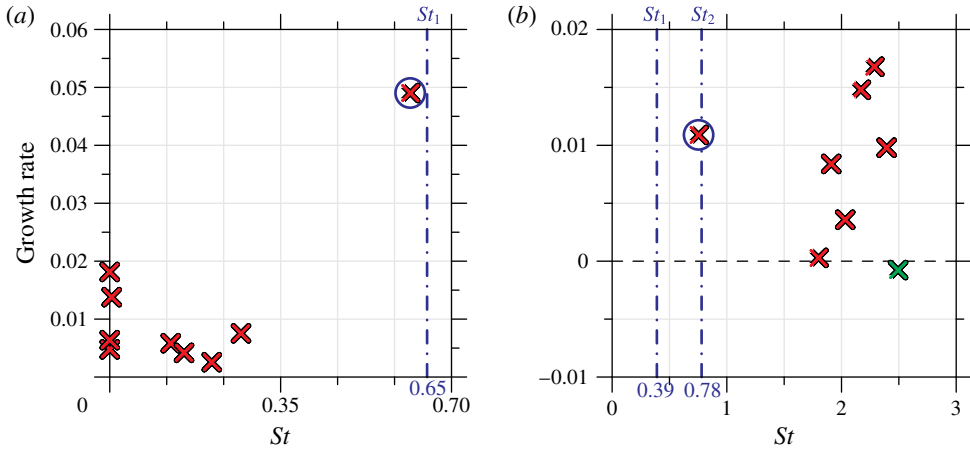
FIGURE 8. (Colour online) GLSA eigenvalue spectrum for the JICF at $Re = 2000$ for $R = 2$ (*a*) and $R = 4$ (*b*). The eigenvalues have been non-dimensionalized so that the growth rate is $\mathrm{Re}(\omega)D/(2\pi v_{jet,max})$ and the Strouhal number is $\mathrm{Im}(\omega)D/(2\pi v_{jet,max})$. The vertical blue dashed lines correspond to most dominant frequencies from DNS vertical velocity spectra results taken from the upstream shear layer by Iyer & Mahesh (2016). The DNS frequency of $St_2 = 1.3$ from Iyer & Mahesh (2016) is not shown in (*a*) as it would obscure the lower-frequency GLSA results. Eigenvalues (ω_j) with red symbols are unstable modes (i.e. positive growth rate), while stable values are coloured green. The circled eigenvalues have their corresponding eigenmodes shown in figure 9 for $R = 2$ (*a*) and $R = 4$ (*b*).

that match the frequencies from vertical velocity spectra. For case $R4$, it is not as clear how the eigenmode and DMD modes compare from figure 9(*b,d,f*) alone. However, the cross-sectional views in figure 10 show that the eigenmode at $St = 0.75$ (figure 10*b*) agrees well qualitatively with the DMD mode at $St = 0.78$ (figure 10*f*).

GLSA for case $R2$ predicts an eigenmode at $St = 0.62$ originating near the jet exit and propagating along the upstream shear-layer. DMD and vertical velocity spectra capture $St = 0.65$ and a higher harmonic at $St = 1.3$ along the upstream shear layer. It is clear from the isometric views in figure 9 that the upstream shear-layer eigenmode at $St = 0.62$ (figure 9*a*) and DMD mode at $St = 0.65$ (figure 9*c*) for case $R2$ agree well qualitatively. Additionally, figure 10 shows good agreement for the cross-section between the eigenmodes and DMD modes when $R = 2$. As expected, GLSA does not predict the nonlinear higher harmonic at $St = 1.3 \approx 0.65 \times 2$.

For the $R4$ case, GLSA predicts an eigenmode at $St = 0.75$ along the upstream shear layer, while DMD and vertical velocity spectra show $St = 0.39$ and an harmonic at $St = 0.78$. Iyer & Mahesh (2016) have shown $St = 0.78$ to include about 43 % of the spectral energy when compared to the most dominant DMD mode ($St = 0.39$). However, note that the DMD mode at $St = 0.78$ presents itself much closer to the nozzle and is clearly a shear-layer mode. $St = 0.39$, on the other hand, has its largest magnitude further downstream and is located between the upstream and downstream shear layers. This can be observed in the cross-sectional view as a part of figure10(*d*).

Rowley *et al.* (2009) compared the JICF GLSA results of Bagheri *et al.* (2009) with DNS and DMD. They showed that GLSA recovers an upstream shear-layer instability mode with a different frequency than what is captured by DNS and DMD. Note that Bagheri *et al.* (2009) computed a steady-state base flow using SFD. Additionally, the jet nozzle was not included in the simulation and top-hat jet exit profile was
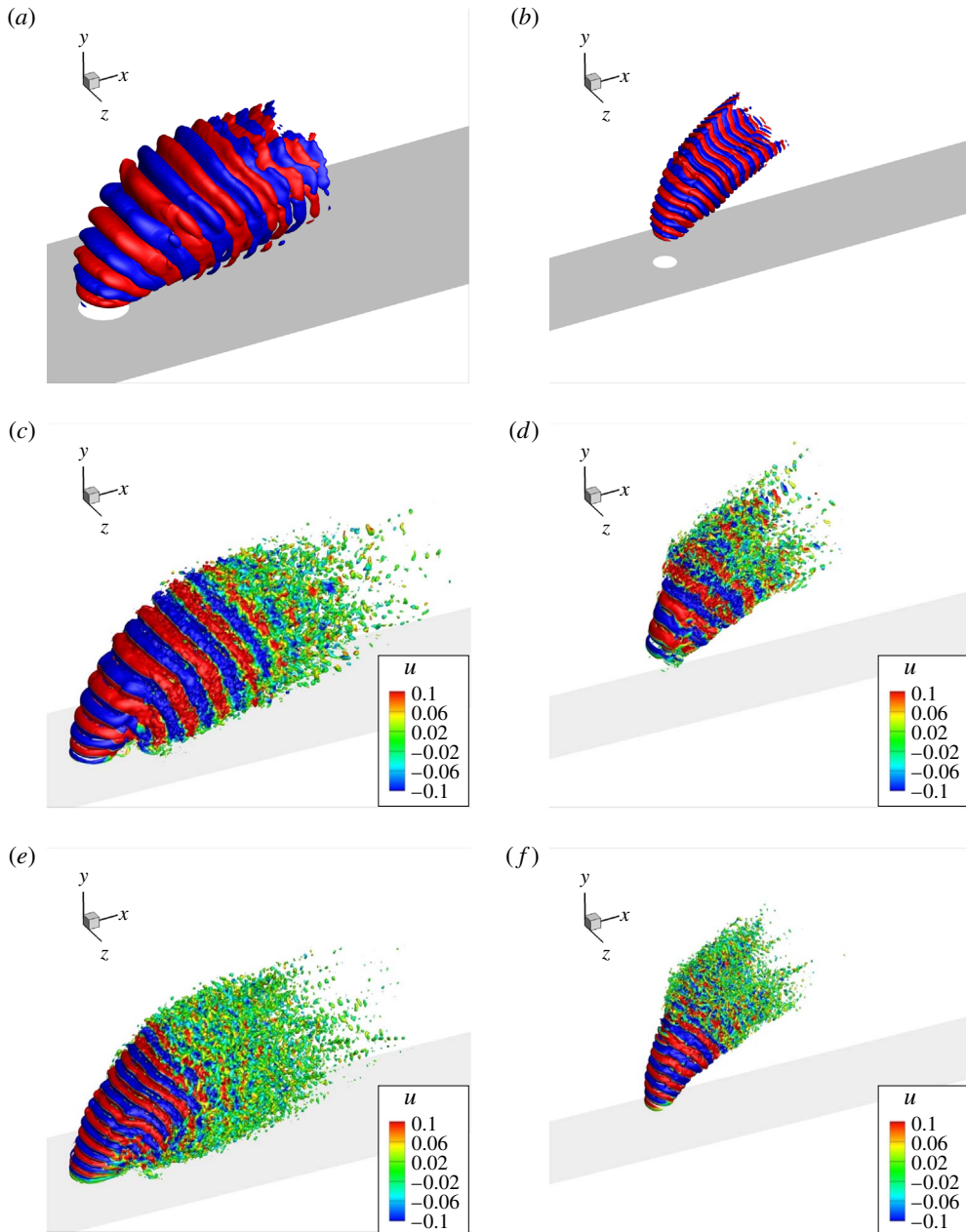
FIGURE 9. (Colour online) Real part of the eigenmodes for case $R2$ at $St = 0.62$ (a) and $R4$ at $St = 0.75$ (b) are shown with positive and negative isocontours of $\tilde{u}$ and $\overline{v}$. Isocontours of Q-criterion for the DMD modes by Iyer & Mahesh (2016) are shown for $R2$ at $St = 0.65$ (c) and $St = 1.3$ (e) and for $R4$ at $St = 0.39$ (d) and $St = 0.78$ (f).

prescribed. Interestingly, the present work has shown that using the turbulent mean flow as the base state in GLSA, the captured upstream shear-layer instability mode has the same frequency as the DNS and DMD results of Iyer & Mahesh (2016).
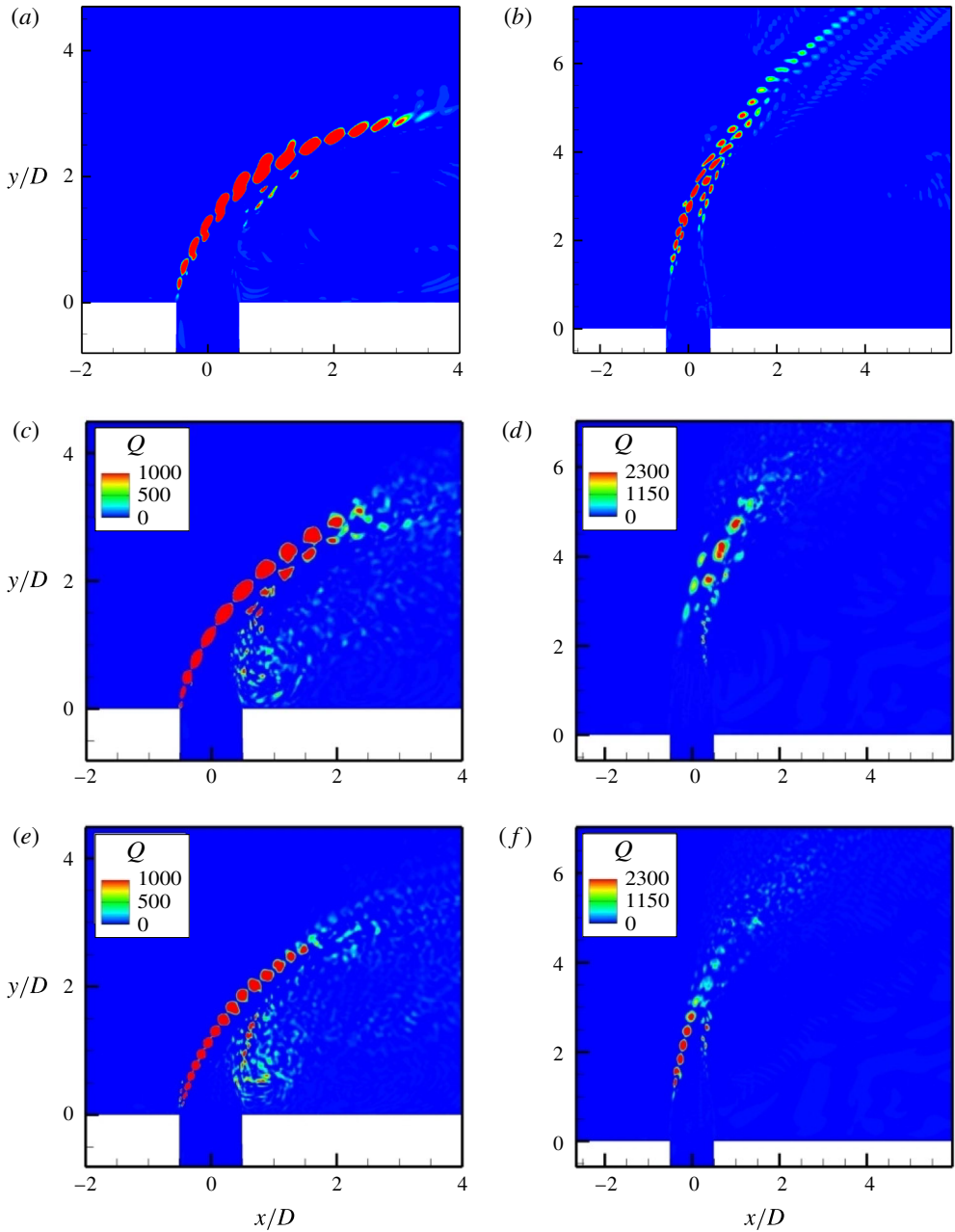
FIGURE 10. (Colour online) Slices of eigenmodes and DMD modes (from Iyer & Mahesh (2016)) at the symmetry plane ($z = 0$) with contours of Q-criterion. The eigenmodes have frequencies of $St = 0.62$ (*a*) and $St = 0.75$ (*b*) for $R = 2$ and $R = 4$, respectively. The DMD modes have frequencies for case $R2$ at $St = 0.65$ (*c*) and $St = 1.3$ (*e*) and case $R4$ at $St = 0.39$ (*d*) and $St = 0.78$ (*f*).
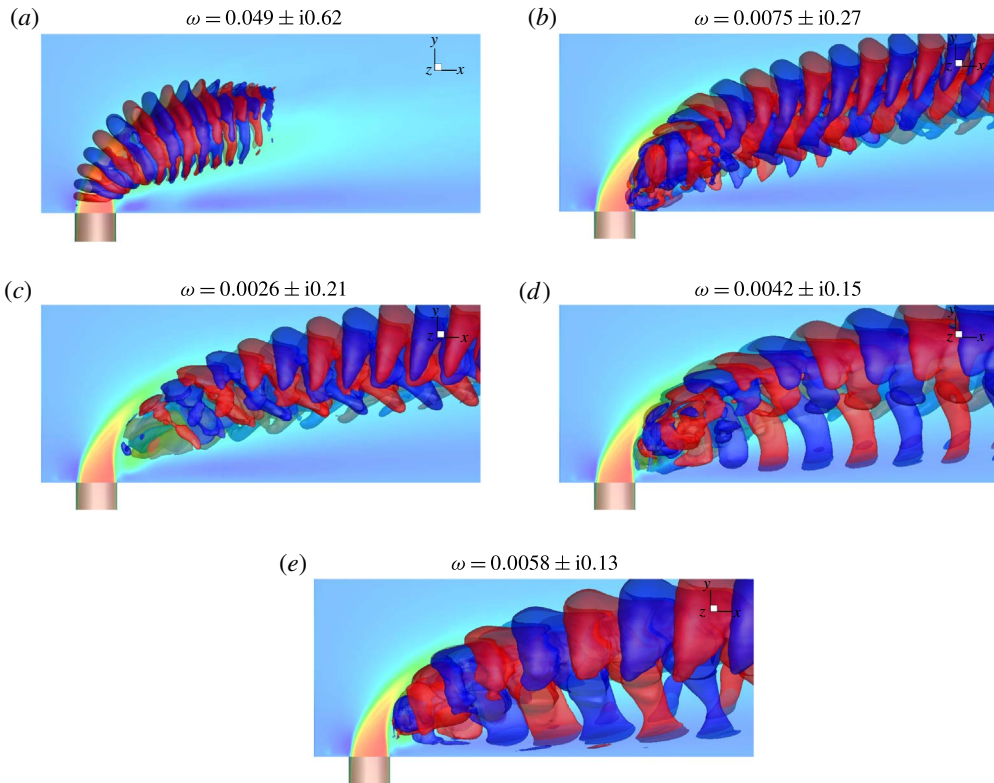
FIGURE 11. (Colour online) Real part of the eigenmodes for case $R2$ are shown with positive and negative isocontours of $\tilde{u}$ and $\overline{v}$ contours of the base state in the background. The eigenvalues are shown above, with the real part being the growth rate, and the imaginary part being the Strouhal number. Mode (*a*) corresponds to the most unstable and highest-frequency upstream shear-layer mode. Modes (*b–e*) are lower frequency and originate near the downstream shear layer and travel far downstream. Modes (*d*) and (*e*) also show a connection between near-wall motions and motions in the jet wake.

5.1. *Stability analysis of R2*

Figure 11 shows the eigenmodes that are associated with the eigenvalues in figure 8(*a*) for case $R2$. To better characterize the eigenmodes, they can be grouped according to their frequencies and spatial structures. For this case, we notice that there are three main groups.

The first group consists of the shear-layer mode seen in figure 11(*a*). This eigenmode oscillates at a frequency very close to what is observed in DNS and experiments. Additionally, it originates near the jet exit at the initiation of the upstream shear layer. Furthermore, this eigenmode extends downstream after the collapse of the potential core while still maintaining a large magnitude. This implies that the eigenmode is growing as it travels downstream but also growing at the jet exit; characteristic of an absolute instability.

Next is the group that occupies a range of lower frequencies that may be identified as the wake modes. This group consists of figure 11(*b–e*). Low frequencies have been shown by Iyer & Mahesh (2016) to include a significant portion of the spectral energy, highlighting their importance and relevance in the overall flow physics for

this configuration. The four wake modes are qualitatively similar, but exhibit different spatial length scales. Additionally, the lower-frequency wake modes highlight the connection between the near wall motions and motions deep in the jet wake. The wake modes originate behind the downstream shear layer after the collapse of the potential core and dominate far downstream. Figure 11(b,c) shows the eigenmodes that persist downstream, but remain in the jet wake. Specifically, the eigenmodes observed in figure 11(d,e) act at the lowest of frequencies for this configuration. The observed frequencies are consistent with notion that Strouhal numbers associated with the jet diameter (D) will be lower than those associated with the shear layer.

Finally, the Reynolds stresses present in the turbulent mean flow show up in GLSA as stationary eigenmodes. This is because the Reynolds stress becomes a steady forcing term in the LNS equations once the base flow equations are subtracted (2.3). The stationary eigenmodes are not relevant to the present analysis and are not included.

5.2. *Stability analysis of R*4

All of the eigenmodes for case $R4$ are shown in figure 12 and are associated with the eigenvalues in figure 8(b). Again, it is convenient to group the eigenmodes. We observe from the spectrum in figure 8(b) and the eigenmodes from figure 12 that there are two main groups.

The high-frequency eigenmodes make up the first group. These eigenmodes are all located along the downstream shear layer. Not much attention has been given to the stability of the downstream shear layer. However, the present work shows that two of the downstream shear-layer modes have higher growth rates than the upstream shear layer, and therefore must not be ignored when considering the stability at $R = 4$. Note that the downstream shear-layer modes occupy a range of frequencies. All of these modes interact with the upstream shear layer at the collapse of the potential core. This may explain why different frequencies are present along the shear layer as seen from upstream shear-layer vertical velocity spectra for $R = 4$.

Case $R4$ has been shown to change its dominant frequencies along the upstream shear layer; conversely to case $R2$. When $R = 4$, the upstream shear-layer eigenmode at $St = 0.75$ originates much further away from the jet when compared to the upstream shear-layer mode of case $R2$. This is consistent with a convective instability where the flow instability travels downstream, but does not grow at the point of origin (i.e. near the jet exit).

6. Summary

A GLSA capability has been developed for studying complex flows with unstructured grids to further study the low-speed JICF. The use of turbulent mean flows for GLSA is justified using a scale-separation argument. GLSA has been shown to successfully capture the upstream shear-layer instabilities at the same Strouhal numbers as those found using DNS and DMD analysis of Iyer & Mahesh (2016) for both cases $R2$ and $R4$. GLSA has also provided supportive evidence for the upstream shear-layer's transition from absolutely to convectively unstable as R increases from 2 to 4. The present work has shown that the downstream shear layer plays an important role in the stability of JICFs at higher R values.

When analysing the entire GLSA spectrum for case $R2$, as shown in figure 8(a), note the eigenvalue with the highest growth rate, which has a frequency of $St = 0.62$. The associated dominant eigenmode observed in figure 9(a) is located along the
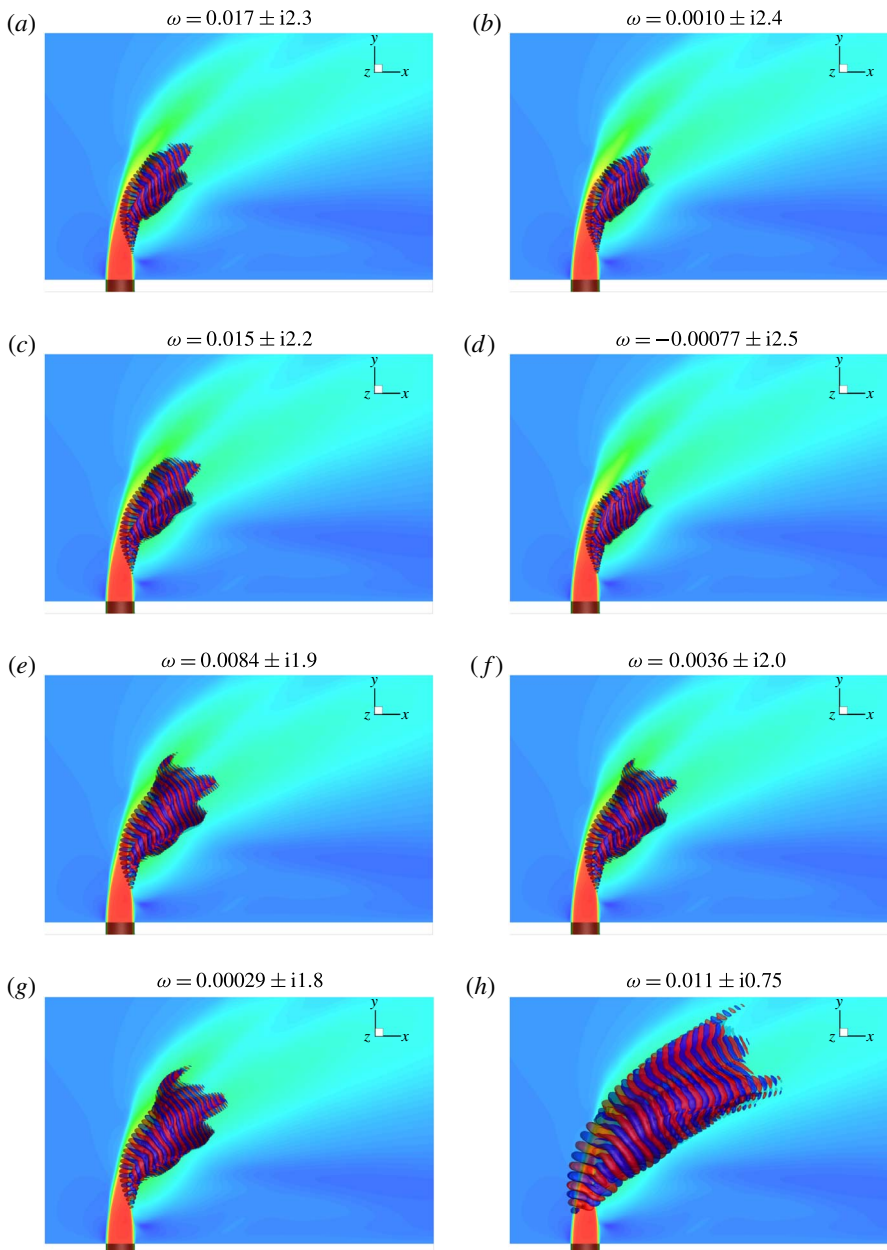
FIGURE 12. (Colour online) Real part of the eigenmodes for case $R4$ are shown with positive and negative isocontours of $\tilde{u}$ and $\overline{v}$ contours of the base state in the background to highlight the jet base flow. The associated eigenvalues are shown above, with the real part being the growth rate and the imaginary part being the Strouhal number. Modes (a–g) correspond to the higher-frequency downstream shear-layer modes. Mode (h) is associated with the upstream shear layer.

upstream shear layer. This sheds light on the most dominant instability for this flow. Leveraging this knowledge by either attempting to dampen or amplify the upstream shear-layer mode near the jet exit has often been an effective control strategy in

other applications. However, note that further downstream, this mode has a dramatic reduction in amplitude, which suggests this mode is only dominant 4–5*D* downstream of the jet orifice. The rest of the GLSA spectrum for $R = 2$ has growth rates less than 30 % of the growth rate for the upstream shear-layer mode, which may convey less relevance to the overall stability. However, after examining the spatial structure of these lower-frequency modes reveals that they continue to have a large impact far downstream. This could be important when attempting to control the JICF. For example, if mixing downstream is important, damping or amplifying these unstable wake modes may be more effective than trying to control the upstream shear-layer instability. Note that the origin of the wake modes appears to be slightly above the jet orifice, which makes it unclear how effective actuation in the nozzle or near the jet orifice may be.

For case $R4$, again note that GLSA has been shown to capture the relevant flow physics in § 5. Unlike the $R2$ case, the GLSA spectrum for case $R4$ in figure 8(*b*) shows that the most unstable eigenvalue is not associated with the upstream shear layer. Instead, the most unstable eigenvalue sits on the downstream shear layer, and is accompanied by a range of other eigenvalues also located along the downstream shear layer. These downstream shear-layer eigenvalues have a range of Strouhal numbers from approximately 1.7–2.5. Not much attention has been given to the downstream shear layer in the past, but for higher R values it should not be ignored.

Acknowledgements

REFERENCES

ÅKERVIK, E., BRANDT, L., HENNINGSON, D. S., HŒPFFNER, J., MARXEN, O. & SCHLATTER, P. 2006 Steady solutions of the Navier–Stokes equations by selective frequency damping. *Phys. Fluids* **18** (6), 068102.

ALVES, L. S. DE B., KELLY, R. E. & KARAGOZIAN, A. R. 2008 Transverse-jet shear-layer instabilities. Part 2. Linear analysis for large jet-to-cross-flow velocity ratio. *J. Fluid Mech.* **602** (2008), 383–401.

ARNOLDI, W. E. 1951 The principle of minimized iteration in the solution of the matrix eigenproblem. *Q. Appl. Maths* **9**, 17–29.

BABU, P. C. & MAHESH, K. 2004 Upstream entrainment in numerical simulations of spatially evolving round jets. *Phys. Fluids* **16** (10), 3699–3705.

BAGHERI, S., SCHLATTER, P., SCHMID, P. J. & HENNINGSON, D. S. 2009 Global stability of a jet in cross-flow. *J. Fluid Mech.* **624**, 33–44.

BARKLEY, D. 2006 Linear analysis of the cylinder wake mean flow. *Europhys. Lett.* **75** (5), 750–756.

COELHO, S. L. V. & HUNT, J. C. R. 1989 The dynamics of the near field of strong jets in cross-flows. *J. Fluid Mech.* **200**, 95–120.

CRIGHTON, D. G. & GASTER, M. 1976 Stability of slowly diverging jet flow. *J. Fluid Mech.* **77**, 397–413.

CRIMINALE, W. O., JACKSON, T. L. & JOSLIN, R. D. 2003 *Theory and Computation of Hydrodynamic Stability*. Cambridge Univesity Press.

DING, Y. & KAWAHARA, M. 1998 Linear stability of incompressible flow using a mixed finite element method. *J. Comput. Phys.* **273**, 243–273.

EIFF, O. S., KAWALL, J. G. & KEFFER, J. F. 1995 Lock-in of vortices in the wake of an elevated round turbulent jet in a cross-flow. *Exp. Fluids* **19** (3), 203–213.

FRIC, T. F. & ROSHKO, A. 1994 Vortical structure in the wake of a transverse jet. *J. Fluid Mech.* **279**, 1–47.

GIANNETTI, F., LUCHINI, L. & MARINO, L. 2009 Linear stability analysis of three-dimensional lid-driven cavity flow. In *Proceedings of the 19th Congress of the Italian Association of Theoretical and Applied Mechanics, 14–17 September, 2009, Aras Edizioni, Ancona, Italy*, pp. 738.1–738.10.

GÓMEZ, F., GÓMEZ, R. & THEOFILIS, V. 2014 On three-dimensional global linear instability analysis of flows with standard aerodynamics codes. *Aerosp. Sci. Technol.* **32** (1), 223–234.

HUERRE, P. & MONKEWITZ, P. A. 1985 Absolute and convective instabilities in open shear layers. *J. Fluid Mech.* **159**, 151–168.

HUNT, J. C. R., WRAY, A. A. & MOIN, P. 1988 Eddies, streams, and convergence zones in turbulent flows. *Center for Turbulence Research, Proc. Summer Program (1970)*, pp. 193–208.

IYER, P. S. & MAHESH, K. 2016 A numerical study of shear layer characteristics of low-speed transverse jets. *J. Fluid Mech.* **790** (2016), 275–307.

JORDAN, P. & COLONIUS, T. 2013 Wave packets and turbulent jet noise. *Annu. Rev. Fluid Mech.* **45** (1), 173–195.

JUNIPER, M. P., HANIFI, A. & THEOFILIS, V. 2014 Modal stability theory lecture notes from the flow-nordita summer school on advanced instability methods for complex flows, Stockholm, Sweden. *Appl. Mech. Rev.* **66** (2).

KAMOTANI, Y. & GREBER, I. 1972 Experiments on a turbulent jet in a cross flow. *AIAA J.* **10** (11), 1425–1429.

KARAGOZIAN, A. R. 2010 Transverse jets and their control. *Prog. Energy Combust. Sci.* **36** (5), 531–553.

KELSO, R. M., LIM, T. T. & PERRY, A. E. 1996 An experimental study of round jets in cross-flow. *J. Fluid Mech.* **306**, 111–144.

KELSO, R. M. & SMITS, A. J. 1995 Horseshoe vortex systems resulting from the interaction between a laminar boundary layer and a transverse jet. *Phys. Fluids* **7** (1), 153–158.

KROTHAPALLI, A., LOURENCO, L. & BUCHLIN, J. M 1990 Separated flow upstream of a jet in a cross-flow. *AIAA J.* **28** (3), 414–420.

LEHOUCQ, R. B., SORENSEN, D. C. & YANG, C. 1997 ARPACK Users' Guide: Solution of Large Scale Eigenvalue Problems with Implicitly Restarted Arnoldi Methods.

MAHESH, K. 2013 The interaction of jets with cross-flow. *Annu. Rev. Fluid Mech.* **45** (1), 379–407.

MAHESH, K., CONSTANTINESCU, G. & MOIN, P. 2004 A numerical method for large-eddy simulation in complex geometries. *J. Comput. Phys.* **197** (1), 215–240.

MARGASON, R. J. 1993 Fifty years of jet in cross flow research. *Advisory Group for Aerospace Research & Development Conference*, vol. 534, pp. 1–41.

M'CLOSKEY, R. T., KING, J. M., CORTELEZZI, L. & KARAGOZIAN, A. R. 2002 The actively controlled jet in cross-flow. *J. Fluid Mech.* **452**, 325–335.

MCMAHON, H. M., HESTER, D. D. & PALFERY, J. G. 1971 Vortex shedding from a turbulent jet in a cross-wind. *J. Fluid Mech.* **48** (1), 73–80.

MEGERIAN, S., DAVITIAN, J., ALVES, L. S. DE B. & KARAGOZIAN, A. R. 2007 Transverse-jet shear-layer instabilities. Part 1. Experimental studies. *J. Fluid Mech.* **593**, 93–129.

MOUSSA, Z. M., TRISCHKA, J. W. & ESKINAZI, D. S. 1977 The near field in the mixing of a round jet with a cross-stream. *J. Fluid Mech.* **80** (1), 49–80.

MUPPIDI, S. & MAHESH, K. 2005 Study of trajectories of jets in cross-flow using direct numerical simulations. *J. Fluid Mech.* **530**, 81–100.

MUPPIDI, S. & MAHESH, K. 2007 Direct numerical simulation of round turbulent jets in cross-flow. *J. Fluid Mech.* **574**, 59–84.

MUPPIDI, S. & MAHESH, K. 2008 Direct numerical simulation of passive scalar transport in transverse jets. *J. Fluid Mech.* **598**, 335–360.

NARAYANAN, S., BAROOAH, P. & COHEN, J. M. 2003 Dynamics and control of an isolated jet in cross-flow. *AIAA J.* **41** (12), 2316–2330.

PEPLINSKI, A., SCHLATTER, P. & HENNINGSON, D. S. 2015 Global stability and optimal perturbation for a jet in cross-flow. *Eur. J. Mech. (B/Fluids)* **49**, 438–447.

POPE, S. B. 2000 *Turbulent Flows*, 1st edn. Cambridge University Press.

ROWLEY, C. W., MEZIĆ, I., BAGHERI, S., SCHLATTER, P. & HENNINGSON, D. S. 2009 Spectral analysis of nonlinear flows. *J. Fluid Mech.* **641**, 115–127.

SAU, R. & MAHESH, K. 2007 Passive scalar mixing in vortex rings. *J. Fluid Mech.* **582**, 449.

SAU, R. & MAHESH, K. 2008 Dynamics and mixing of vortex rings in cross-flow. *J. Fluid Mech.* **604**, 389–409.

SCHLICHTING, H. & GERSTEN, K. 1979 *Boundary-layer Theory*, 7th edn. McGraw Hill.

SHAPIRO, S. R., KING, J., M'CLOSKEY, R. T. & KARAGOZIAN, A. R. 2006 Optimization of controlled jets in cross-flow. *AIAA J.* **44** (6), 1292–1298.

SMITH, S. H. & MUNGAL, M. G. 1998 Mixing, structure and scaling of the jet in cross-flow. *J. Fluid Mech.* **357** (1998), 83–122.

TAMMISOLA, O. & JUNIPER, M. P. 2016 Coherent structures in a swirl injector at $Re = 4800$ by nonlinear simulations and linear global modes. *J. Fluid Mech.* **792**, 620–657.

THEOFILIS, V. 2011 Global linear instability. *Annu. Rev. Fluid Mech.* **43** (1), 319–352.

TURTON, S. E., TUCKERMAN, L. S. & BARKLEY, DWIGHT 2015 Prediction of frequencies in thermosolutal convection from mean flows. *Phys. Rev.* E **91** (4), 1–10.

VYAZMINA, E. 2010 Bifurcations in a swirling flow. PhD thesis, École Polytechnique.